Q. J. R. Meteorol. Soc. (1999), **125**, pp. 1–999

Fast and Slow Kelvin Waves in the Madden-Julian Oscillation of a GCM

By ADRIAN. J. MATTHEWS,[1]* JULIA. M. SLINGO,[1] BRIAN. J. HOSKINS[1] and PETER. M. INNESS[2]

[1] *University of Reading, UK*
[2] *Meteorological Office, UK*

(Received 9 February 1998; revised 22 June 1998)

Summary

The structure of the Madden-Julian Oscillation (MJO) in an 1800-day integration of the Hadley Centre Unified Model was analysed, and interpreted within a Kelvin wave framework. The model was forced with constant equinoctial (March) boundary conditions so that a "clean" MJO signal could be separated from the effects of the seasonal cycle and forced interannual variability. The simulated MJO was fairly realistic in terms of its large-scale spatial structure and propagation characteristics, although its period of 30 days (corresponding to an average phase speed of 15 m s^{-1}) was shorter than that observed. The signal in deep convection was less coherent than in observations, and appeared to move eastward as a sequence of discrete convective anomalies, rather than by a smooth eastward propagation. Both "fast" and "slow" equatorial Kelvin waves appeared to play an important role in the eastward propagation of the simulated MJO. Enhanced convection over the Indian Ocean was associated with a "fast" equatorial Kelvin wave that propagated eastward at 55 m s^{-1} over the Pacific. On reaching the west coast of South America, a component of this Kelvin wave propagated northward and southward as a trapped wave along the mountain ranges of Central America and the Andes, in agreement with observations. The anomalous surface easterlies over the tropical eastern Pacific associated with this fast Kelvin wave enhanced the climatological mean easterlies and led to positive convective anomalies over the eastern Pacific consistent with the WISHE mechanism. However, WISHE was not able to account for the eastward development of the convective anomalies over the Indian Ocean/western Pacific region. By splitting the equatorial divergence anomalies of the simulated MJO into their $\partial u/\partial x$ and $\partial v/\partial y$ components, the role of Kelvin wave dynamics in the "slow" (15 m s^{-1}) average eastward propagation of the simulated MJO was examined. Although the two components were of comparable magnitude, the $\partial u/\partial x$ component exhibited a pronounced eastward propagation which tended to be disrupted by the $\partial v/\partial y$ component, thus supporting the paradigm of an underlying, but strongly modified, Kelvin wave mechanism.

KEYWORDS: Madden-Julian oscillation Kelvin wave WISHE General Circulation Model

1. INTRODUCTION

The Madden-Julian Oscillation (MJO) can be characterised by an eastward-propagating planetary-scale tropospheric wave in the tropics with a time-scale between 30 and 60 days. Such a wave can be identified in many fields, including the divergent and rotational wind fields, temperature and surface pressure. As the upper-level divergent part of this wave passes over the convectively active regions of Africa, the warm pool, and South America, convection is enhanced, but there is relatively little convective signal over the eastern Pacific and the Atlantic (e.g., Madden and Julian 1972; Knutson and Weickmann 1987; Rui and Wang 1990; Hendon and Salby 1994). A current paradigm of the MJO is one of a slow Rossby-Kelvin wave over the convectively active Eastern Hemisphere and a faster Kelvin wave over the dry Western Hemisphere. The MJO also has an extratropical component; in northern winter a wavetrain emanates from the warm pool region and arcs over the North Pacific and North America. This can be interpreted in terms of a Rossby wave response to the enhanced convection over the warm pool region (Ferranti *et al.* 1990; Hsu *et al.* 1990).

An analogue of the MJO can be identified in many atmospheric General Circulation Models (GCMs). In a study of 15 GCM integrations as part of the Atmospheric Model

* Corresponding author: CRC Southern Hemisphere Meteorology, Monash University, Wellington Road, Clayton, Vic 3168, Australia. E-mail: ajm@vortex.shm.monash.edu.au

Intercomparison Project (AMIP), Slingo *et al.* (1996) identified several general characteristics of the MJO as simulated by GCMs. While most models showed evidence of eastward-propagating anomalies on intraseasonal timescales, the period of these oscillations tended to be shorter than that observed. In addition, most models underestimated the strength of the intraseasonal variability and did not show evidence of the seasonality of the oscillation. Using the variance of the 200-mb mean zonal wind on timescales of 20-100 days as an indicator of the strength of the MJO, the UK Meteorological Office (UKMO) GCM, or Unified Model (UM), was found to have one of the strongest MJOs.

The characteristics of the MJO change considerably between seasons (e.g., Knutson and Weickmann 1987). This can be attributed (at least partly) to changes in the basic state and forcing patterns of solar insolation and Sea Surface Temperature (SST). Interannual variability also presents a problem in the analysis of the MJO. During El Niño, or "warm event" years the mean and anomalous convective maxima tend to be shifted eastward from the western Pacific towards the central Pacific. Therefore, to obtain a "clean" MJO signal, the UM was integrated with constant boundary conditions for 1800 days. Such constant boundary conditions removed the variability associated both with the seasonal cycle and the interannual SST variability from the analysis of the MJO.

The MJO has its maximum amplitude around February and March (Salby and Hendon 1994; Slingo *et al.* 1996). For the purposes of an extended integration of a GCM with constant boundary conditions, equinoctial boundary conditions may be preferred, as the forcing by solar insolation will be symmetric about the equator and there may not be such a tendency for the mean climate to drift. This paper describes the structure of the MJO in a perpetual March integration of the UM. Comparisons with observations, and other model simulations, particularly the AMIP integration of the UM over the 1979-88 decade are made. The basic mechanisms behind the MJO are discussed, and suggestions to improve the simulation of the MJO are made. Such improvements would be hoped to enhance medium range prediction on the one-week to two-month timescale. By "MJO" an eastward-propagating tropical mode with a time-scale between 20 and 70 days is understood, although the simulated MJO may differ significantly from the observed MJO in terms of its detailed structure, and propagation and maintenance mechanisms.

2. Model Integration and Validation Data

Cullen (1993) gives an overview of the UM, and a description of the "HADAM2b" version used in this study can be found in Inness and Gregory (1997). The UM is a gridpoint model, with a resolution of 3.75° longitude and 2.5° latitude. There are 19 hybrid vertical levels; terrain-following sigma levels near the surface smoothly merge with pressure levels. A comprehensive physics package is included. The convection parametrization scheme is based on the mass flux scheme of Gregory and Rowntree (1990), which is closed on buoyancy, and has a representation of convective downdraughts. As a general rule, Slingo *et al.* (1996) found that models whose convective parametrization schemes closed on buoyancy, rather than moisture convergence, tended to produce realistic mean precipitation patterns that followed SST patterns, and had more realistic simulations of the MJO.

The average March 1 boundary conditions from the UM AMIP integration were chosen as the constant boundary conditions for this integration. These constant boundary conditions were solar insolation, SST, surface albedo, ozone, and sea ice fraction and depth. Soil moisture and snow depth were also kept constant to avoid an excessive drift

in land surface temperature. The model was integrated for 1800 days and daily averaged data were calculated from 6-hourly fields.

The model climatology was validated against OLR data from NOAA polar orbiting satellites (Liebmann and Smith 1996), and circulation data from the NCEP/NCAR reanalyses (Kalnay *et al.* 1996), both as daily averages on a 2.5° x 2.5° grid. A 199-weight 20-100 day bandpass Lanczos filter (Duchon 1979) was used to filter some of the data. The filter response was approximately unity for periods between 23 and 62 days.

3. Model Climatology

As the MJO can be viewed as a modulation of the basic state, some climatological fields of the model were first assessed against observations. Climatological mean OLR from the model integration (Fig. 1a) is shown with mean February-March satellite OLR (1979-95) (Fig. 1b). In the Pacific, the simulated InterTropical Convergence Zone (ITCZ) and South Pacific Convergence Zone (SPCZ) are in the correct position in the model, but show lower OLR values (more intense convection) than the satellite climatology. Tropical convection over Africa, the Indian Ocean, and South America is reasonably well represented in the model, if a little weaker than in the observations. However, there is a large discrepancy between the model and satellite climatologies over the warm pool region. The satellite climatology (Fig. 1b) indicates an extensive region of deep convection over Indonesia and the western Pacific with OLR values less than 220 W m^{-2}. However, the mean OLR from the UM integration (Fig. 1a) in this region is near 260 W m^{-2}, indicating much less intense convection than that observed. This weaker simulated mean convection over the warm pool is likely to have significant implications for the structure of the simulated MJO.

The simulated climatological zonal wind at 200 mb (Fig. 1c) can be compared with a February-March 200-mb zonal wind climatology calculated from 17 years (1979-95) of NCEP/NCAR reanalyses (Fig. 1d). The extent and strength of the simulated tropical mean easterlies and the westerly duct in the eastern Pacific, with westerlies in excess of 10 m s^{-1}, are in good agreement with the reanalysis climatology, although the simulated mean easterlies over the Pacific extend further eastwards (to 130°W) in the Southern Hemisphere than in the observed field. The position and strength of the simulated Northern Hemisphere subtropical jet is also realistic, especially over North America and the Middle East. The simulated East Asian jet maximum, though of the correct magnitude, is situated further northeast than in observations. The simulated Southern Hemisphere jet is slightly stronger than in the observations, and does not show the split jet structure near New Zealand. The extratropical part of the MJO can be interpreted as Rossby wave propagation on a climatological mean flow. As the propagation characteristics of the Rossby waves will depend crucially on the structure of the mean flow, this generally well simulated mean flow is highly desirable.

An alternative measure of the mean flow that is directly relevant to Rossby wave propagation is Potential Vorticity (PV). Figures 1e,f show the climatological mean PV fields on the 350 K isentropic surface (which is at approximately the 200-mb level) for the model simulation and from observations, respectively. The two fields are similar but the PV gradients are stronger in the simulation (Fig. 1e), both in the Northern and Southern Hemispheres. Therefore it is anticipated that the simulated MJO will have a strong extratropical component.

4. Equatorial Propagation of Simulated Intraseasonal Anomalies

(*a*) *Spectral Analysis*

The simulated MJO is first evaluated by an examination of the planetary-scale equatorial divergence field, as the observed MJO can be characterised by an eastward-propagating zonal wavenumber one equatorial wave in velocity potential (e.g., Lorenc 1984). Spectral analysis of the 200-mb equatorial velocity potential fields from the perpetual March integration, averaged from 10°N to 10°S, showed that the zonal wavenumber one component accounted for 58% of the variance, far more than any other wavenumber. For comparison, power spectra of zonal wavenumber one 200-mb equatorial velocity potential from the 10 year (3600 day) UM AMIP integration and from 10 years (3652 days) of NCEP/NCAR reanalyses over the AMIP period have also been computed.

Prior to computation of the power spectra, the mean and linear trend were removed from the time series at each longitude, and a 10% cosine taper applied. The first three harmonics of the annual cycle were also removed from the UM AMIP integration and the NCEP/NCAR reanalyses. Finally all three spectra were smoothed to have approximately the same spectral bandwidth of $\Delta f \approx 0.004$ day^{-1}.

All three spectra show substantially more power at positive frequencies (Fig. 2), indicating the dominance of eastward-propagating waves over westward-propagating waves. The NCEP/NCAR reanalysis (Fig. 2a) has a large peak at the lowest, interannual, frequencies, due to ENSO variations, and peaks of eastward-propagating intraseasonal waves with periods near 40 and 60 days, with relatively little power at intermediate timescales.

The UM AMIP integration (Fig. 2b) has a similar, but smoother, red spectrum to the reanalysis, but with less power at intraseasonal timescales. Also, the intraseasonal peaks tend to be at slightly higher frequencies in the AMIP integration, with periods between about 30 and 60 days.

The UM perpetual March integration does not show a red spectrum (Fig. 2c). The strongest peak has a period near 30 days, which corresponds to a peak in the UM AMIP spectrum. There is a weaker peak near 0.008 day^{-1} (period of 125 days) but there is very little power at lower "interannual" frequencies, as expected.

The statistical significance of the intraseasonal spectral peaks is discussed briefly below. The number of degrees of freedom, ν, associated with each spectral peak, is $\nu \approx 0.873$x2L (Madden and Julian 1971), where the raw spectrum was averaged over L adjacent frequencies. For a particular spectral peak to be significant at the 95% level, it must exceed the background spectrum by a factor of 1.75 for the perpetual March integration with L=7, $\nu \approx 12$, and by a factor of 1.50 for the AMIP integration and the reanalyses with L=15, $\nu \approx 26$. The choice of background spectrum is rather arbitrary. For the AMIP integration and the NCEP/NCAR reanalyses, a red noise background may be appropriate, but for the perpetual March integration a white noise background may be more suitable. Because of this subjectivity, strict statistical significance above a particular theoretical background model has not been shown. However, for any reasonable background spectra fitted by eye, it can be seen that the intraseasonal peaks in the NCEP/NCAR reanalyses do exceed the background by a factor of 1.50 and are therefore significant at the 95% level. However, the intraseasonal peaks in the AMIP integration are probably not significant. The 30-day peak in the perpetual March integration exceeds any reasonable background spectrum by a factor of 1.75 and is therefore also significant at the 95% level.

Hence it appears that the perpetual March integration has been successful in that it has reproduced a distinct MJO-type signal. The period of the simulated MJO is around 30 days, which is shorter than that of the observed MJO, in line with other GCM simulations. There is a marked difference between the power spectra of the UM perpetual March

integration and that of the UM AMIP integration. The perpetual March integration has very little power at low "interannual" frequencies, which is to be expected as there is no "interannual" boundary forcing. However, there is also significantly less power at both the low- and high-frequency end of the intraseasonal band (periods around 50 days and around 20 days) in the perpetual March integration compared to the AMIP integration. This difference in the spectral characteristics of the simulated MJO may be due to the absence of either the annual cycle or the interannual boundary forcing in the perpetual March integration, and may provide a clue to the general property of simulated MJOs having too high a frequency. Accurate simulation of the seasonal cycle and/or interannual variability may be a factor in simulating the correct frequency of the MJO. Alternatively, the greater power at the higher frequencies in the AMIP integration may be associated with intraseasonal behaviour in the other seasons, e.g., the known 10-20 day timescales for the Asian Summer Monsoon. However, the perpetual March integration has produced an MJO with a clearly significant spectral peak. The structure of this simulated MJO can now be analysed without the complicating factors of modification by a seasonal cycle or interannual ENSO variability.

(*b*) *Temporal Behaviour*

Figure 3 shows the time-longitude diagram of 20-100 day filtered 200-mb equatorial velocity potential from the perpetual March integration. Consistent with the spectral analysis, eastward-propagating anomalies can clearly be seen. The anomalies are predominantly zonal wavenumber 1 and propagate around the equator in about 30 days, corresponding to a phase speed of about 15 m s^{-1}.

This 30-day equatorial wave does not appear to be a ubiquitous feature throughout the 1800-day integration. For example, there is little evidence of any eastward-propagating anomalies between days 900 and 1000. Such sporadic behaviour was also found in the simulated MJO of a perpetual January integration (Slingo and Madden 1991). The observed MJO is subject to substantial interannual modulation, being absent in some seasons. The low-frequency modulation of the simulated MJO may be related to this observed interannual variability, but it should be emphasised that in this integration the forcing external to the atmosphere is constant, and therefore the low-frequency variability must be internally generated.

5. Global Structure of the Simulated MJO

(*a*) *EOF Analysis*

The results of the previous section indicated that there is a coherent eastward-propagating wave in the upper-tropospheric equatorial velocity potential field with a period of about 30 days. The associated global structure is now identified using EOF analysis (e.g., Lorenc 1984). The first two eigenvectors of the covariance matrix of 20-100 day filtered 200-mb velocity potential account for 28.3% and 21.8% of the 20-100 day variance, respectively. Hence their structures describe the predominant mode of variability on the 20-100 day time-scale (the third and fourth eigenvectors only account for 15.8% and 5.2% of the variance, respectively). EOF1 (Fig. 4a) has a mainly zonal wavenumber 1 structure, with a minimum over the equatorial western Pacific, corresponding to planetary-scale 200-mb anomalous divergence and inferred enhanced convection. It has a double maxima, corresponding to 200-mb anomalous convergence and reduced convection, over the convectively active regions of the Amazon and equatorial Africa. The

structure of EOF2 (Fig. 4b) is also approximately zonal wavenumber 1, and is shifted westwards relative to that of EOF1, such that it has a minimum over the tropical Indian Ocean. These EOF structures are similar to those calculated from ECMWF analyses for the December-February and the March-May seasons from 1983-89 (Matthews 1993), except in December-February EOFs 1 and 2 are reversed, with EOF1 describing anomalous convection over the Indian Ocean, and EOF2 related to anomalous convection over the western Pacific.

The principal component time series of EOF1 and EOF2, denoted by PC1 and PC2 respectively, are shown in Fig. 5. These show the projection of the EOF spatial structures onto the 20-100 day filtered 200-mb velocity potential field at any time. Both PC1 and PC2 vary with a typical period of around 30 days, and they are highly correlated, such that PC2 leads PC1 by approximately a quarter of a cycle (the maximum correlation coefficient is 0.65 at a lag of 7 days). Finally, a comparison of PC1 and PC2 and the equatorial structures of EOF1 and EOF2 with the time-longitude diagram of Fig. 3 show that the first two EOFs of velocity potential do indeed describe the 30-day velocity potential wave, or simulated MJO. Inspection of Figs. 3 and 5 indicate there are approximately 40 eastward-propagating events in the 1800-day integration. In the next section, PC1 is used as the basis for constructing a life cycle of the simulated MJO.

(*b*) *Regression Analysis*

(i) *Method*

To determine the behaviour of other fields in the simulated MJO, regression maps were constructed for a selection of meteorological variables. For a particular time lag, at each grid-point, a linear regression was performed between the (20-100 day filtered) variable in question and the reference time series of PC1. Figure 5 shows that a typical peak value of the reference time series (PC1) is 2.0. The regressed value of the filtered variable corresponding to PC1=2.0 is then plotted at that grid point. A sequence of such lagged regression maps shows the temporal evolution of the simulated MJO. To cover a whole MJO life cycle, regression maps are shown for lags of -15 days through to +15 days.

The local and global (field) significance of the regression maps were assessed (Livezey and Chen 1983). For a particular regression map, the correlation coefficient between the reference time series and the time series at each grid-point was tested for significance at the 95% level. Temporal correlation was accounted for by using an effective number of degrees of freedom calculated from a decorrelation time-scale between the reference time series and the grid-point time series. As the data have a finite (temporal) length, and are spatially correlated, the field significance of the regression map was then assessed by performing 1000 Monte Carlo simulations. For each simulation, a randomly generated reference time series was regressed against the field variable, and the fractional area of the globe that was locally significant was calculated. A histogram of the frequency distribution of the fraction of locally significant area was built up from the 1000 Monte Carlo simulations. The median value of the histogram is near 5%, and the histogram has a certain spread about this median value due to the spatial correlations in the data. All of the regression fields described in this paper had a percentage of locally significant area that was greater than the 99th percentile of the histogram from their associated Monte Carlo simulation. Therefore, all regression fields are globally significant at the 99% level.

(ii) *Divergent Circulation and Convection*

Figure 6 shows regression maps of 20-100 day filtered 200-mb velocity potential and OLR anomalies, throughout the simulated MJO life cycle. All the features described

below are locally and globally statistically significant. The Day 0 (−8) map of 200-mb velocity potential is very similar to the structure of EOF1 (EOF2) of 200-mb velocity potential, as expected. The 200-mb velocity potential pattern is predominantly zonal wavenumber one, and moves steadily eastward throughout the life cycle, completing a circuit of the globe between Days −15 and +15. Regression maps of 850-mb velocity potential (not shown) have a very similar structure to the corresponding 200-mb patterns, but with opposite sign, indicating a first-internal mode structure in the tropics, with lower-tropospheric convergence and upper-tropospheric divergence and implied mid-tropospheric ascent, in agreement with observations.

The OLR anomalies are consistent with the 200-mb velocity potential anomalies, in that negative (darkly shaded) OLR anomalies, which are indicative of enhanced deep convection, are coincident with negative 200-mb velocity potential anomalies, or regions of deep anomalous ascent. Regression maps of total precipitation rate (not shown) have very similar patterns to those of OLR, confirming that the model OLR is indeed a suitable proxy for deep convection.

However, the OLR anomalies do not show the steady eastward propagation of the velocity potential anomalies. Rather, individual convective anomalies tend to grow and decay in situ (e.g., over the Indian Ocean from Day −15 to Day −4). New anomalies develop to the east of the previous anomaly, with the effect that an envelope of convection moves eastward. The incoherent nature of the eastward development of the OLR anomalies in GCMs as compared to observations was also noted in studies of the MJO in the AMIP integrations of both UKMO and Goddard Laboratory for Atmospheres models (Sperber *et al.* 1997) and may be a common feature of GCM simulations.

A space-time spectral analysis of the equatorial (10°N-10°S) OLR data similar to that in Fig. 2 for the 200-mb velocity potential data confirms the discrete nature of the OLR anomalies in the perpetual March integration. There is approximately equal variance in the westward- and eastward-propagating intraseasonal OLR perturbations for zonal wavenumbers 1-4, indicative of a standing oscillation in OLR. This is in contrast to a space-time spectral analysis of observed intraseasonal OLR data (Zhang and Hendon 1997) which shows a strong predominance of eastward- over westward-propagating perturbations.

The OLR anomalies show many similarities to those in the observed MJO. For example, on Day 0 there is a convective dipole, with enhanced convection over the western Pacific and reduced convection over the Indian Ocean. Half a cycle earlier, at Day −15, the dipole is in its opposite phase. This convective dipole is well established as part of the observed MJO (e.g., Lau and Chan 1983; Knutson and Weickmann 1987).

By definition, OLR anomalies only occur over regions of significant mean convection. In particular there are only small OLR anomalies over the maritime continent itself, consistent with the weakness of mean convection in this region (Fig. 1a). This is in contrast to the observed MJO, which shows large OLR anomalies over the maritime continent (e.g., Knutson and Weickmann 1987). Over the Indian Ocean, the OLR anomalies tend to lie on the poleward edges of the region of mean convection. For example, on Day −8, there is enhanced convection around 5°N and 20°S but little convective anomaly at 10°S. This is in contrast to observations, where the strongest convective anomalies are coincident with the strongest mean convection. Over the Pacific, the OLR anomalies are coincident with the mean convective regions. For example, on Days 0 and +4 the ITCZ north of the equator and the SPCZ are both in a state of enhanced convection.

(iii) *Rotational Circulation*

Figure 7 shows the regression fields for 200- and 850-mb streamfunction and locally

significant wind vector anomalies. Comparison with the OLR anomalies of Fig. 6 shows that a pair of anomalous 200-mb subtropical anticyclones lies to the west of the enhanced convection, and moves eastward from Africa at Day −12 through to Indonesia at Day 0 and 150°E in the western Pacific at Day +8. At this time the Southern Hemisphere anticyclone disappears but the Northern Hemisphere anticyclone can be traced further eastward to the dateline by Day +15. On Day −15 (of the next cycle) the Northern Hemisphere anticyclone is again found at the dateline and moves eastward to 150°W in the central Pacific by Day −12, where it decays by Day −8. This behaviour is very similar to the observed MJO in northern winter (e.g., Knutson and Weickmann 1987). Similarly, a pair of anomalous 200-mb subtropical cyclones lie to the west of the reduced convection, e.g., at 135°E on Day −12.

On Day −4 a 200-mb extratropical wavetrain appears to emanate from the Northern Hemisphere cyclonic anomaly at the dateline. The wavetrain is stationary and amplifies considerably by Day 0, with an anticyclonic centre over the North Pacific, a cyclonic anomaly centred over the western United States with cyclonic curvature extending northwards into Canada, and an anticyclonic anomaly over the eastern United States. The wavetrain is still present at Day +4, but decays by Day +8, and then reappears on Day +12 in its opposite phase as the tropical anticyclonic anomaly moves into the western Pacific. This wavetrain qualitatively resembles the PNA pattern (Barnston and Livezey 1987) and the wavetrain found in observations of the MJO (e.g., Lau and Phillips 1986) but the centres of the wavetrain are somewhat shifted from the observations. This is likely to be due to the different characteristics of the intraseasonal convective anomalies over the warm pool, and the difference in position of the East Asian jet, between the UM simulation and observations. There is also a cyclonic anomaly over the subtropical Atlantic, centred at 20°N, 60°W on Day 0. This may have arisen from the extratropical wavetrain over North America propagating equatorwards through the upper-tropospheric mean westerlies that extend to the equator over the Atlantic (Fig. 1c) and/or it may be associated with the negative convective anomalies over tropical South America (Fig. 6).

In the tropics 850-mb wind and streamfunction anomalies tend to be of opposite sign to 200-mb anomalies, implying a baroclinic structure, in agreement with observations. For example, on Day 0, there are 850-mb westerly anomalies below 200-mb easterly anomalies over the equatorial Indian Ocean, and 850-mb easterly anomalies below 200-mb westerly anomalies over the equatorial Pacific Ocean. Additionally, there is a tendency for an 850-mb subtropical cyclone (anticyclone) pair below the 200-mb anticyclone (cyclone) pair.

In the extratropics poleward of approximately 30°, the 850-mb wind anomalies tend to be in phase with the 200-mb anomalies, again in agreement with observations. In particular, an 850-mb anticyclonic anomaly covers most of the North Pacific from Day −4 to Day +4. This is the lower-tropospheric counterpart of the 200-mb extratropical wavetrain discussed above. Together with the 200-mb wavetrain, this structure appears with reversed sign (an 850-mb cyclonic anomaly over the Pacific) from Day +12 to +15.*

An extratropical wavetrain can also be seen in the Southern Hemisphere. A 200-mb cyclonic anomaly moves eastward along 50°S in the sector from 90°E to 135°E between Day −12 and Day 0 (Fig. 7). By Day +4 downstream dispersion is evident along an approximate great circle route, with the original cyclonic anomaly decaying and an anticyclonic anomaly developing at 45°S, 180°, and a cyclonic anomaly at 30°S, 160°W. This wavetrain has a large area of statistically significant wind anomalies and is stronger

* Although the extratropical streamfunction anomalies at 200 mb and 850 mb may not have the same sign, e.g. at 45°N, 135°W on Day 0, the curvature of the streamfunction anomalies and the wind vector anomalies are of the same sign.

than Southern Hemisphere wavetrains in observational studies of the MJO (Knutson and Weickmann 1987, Kiladis and Weickmann 1992). This may be due to the larger climatological PV gradients in the Southern Hemisphere in the simulation compared to observations (Fig. 1e,f). The phase of the simulated Southern Hemisphere wavetrain also differs from observations. This may be expected, given the different characteristics of the MJO convective anomalies between the simulation and observations.

The simulated MJO shows many similarities to observations; in particular it is consistent with the paradigm of a convectively active equatorial Rossby-Kelvin mode over the Eastern Hemisphere with an associated extratropical wavetrain over the Pacific and North America.

6. Fast Equatorial Kelvin Wave Structures

Figure 8 shows regression maps of OLR and mean Sea Level Pressure (SLP) anomalies for five selected phases of the simulated MJO (Days -10, -8, -6, -4 and 0). Focusing on the tropics, on Day -10 there is enhanced convection (negative OLR anomalies) and negative SLP anomalies over the Indian Ocean, together with reduced convection over the western Pacific and positive SLP anomalies over the whole tropical Pacific. The enhanced convection over the Indian Ocean will tend to be associated with a "positive" Kelvin wave, with negative SLP anomalies to the east, while the reduced convection over the western Pacific will be associated with a "negative" Kelvin wave, with positive SLP anomalies to the east (Heckley and Gill 1984). Hence over the central Pacific, which is to the east of both the positive and negative convective anomalies, there will be a partial cancellation between the two Kelvin waves of opposite sign. By Day -8, the reduced convection over the western Pacific has disappeared, and the "positive" Kelvin wave (equatorially trapped negative SLP anomaly), associated with the enhanced convection over the Indian Ocean, propagates eastward along the equator into the central Pacific. By Day -6 the Kelvin wavefront has reached the western coast of South America.

The average speed of propagation across the whole Pacific is about 55 m s^{-1}. This corresponds approximately to the phase speed of a first-internal vertical mode dry Kelvin wave (e.g., Millif and Madden 1996) and is much faster than the average phase speed of 15 m s^{-1} of the simulated MJO. The negative equatorial SLP anomaly has a corresponding signal in the zonal wind field that is also characteristic of a Kelvin wave. On Day -12, before the SLP signal has begun to cross the Pacific, the regression map of 850-mb streamfunction (Fig. 7) shows little signal over the equatorial Pacific. By Day -8, there are large 850-mb equatorial easterly anomalies over the western Pacific to 150°W, which are in phase with the SLP signal which has also reached 150°W. By Day -4, both the negative SLP and the 850-mb easterly anomalies extend to South America. At 200 mb on Day -4, there are equatorial westerly anomalies over the whole Pacific, confirming the first-internal mode vertical structure.

When the Kelvin wavefront reaches the western coast of South America on Day -6, it feels the influence of the Andes mountain range. The Andes appear to act as a permeable barrier to the Kelvin wave. Some of the equatorial Kelvin wave signal "leaks" over the Andes and continues to propagate eastward along the equator over South America by Day -4 and over the Atlantic and Africa by Day 0. Negative SLP anomalies also propagate southwards along the edge of the Andes, and to a lesser extent, northwards along the edge of the mountains of Central America and Mexico. This behaviour is consistent with observed Kelvin pulses related to Atmospheric Angular Momentum (AAM) oscillations on the MJO time-scale (Weickmann *et al.* 1997). These SLP anomalies may be "coastal"

Kelvin waves, trapped against the side of the mountain ranges, much as an oceanic coastal Kelvin wave is trapped against the coastal topography.

Regression fields of 200-mb geopotential height anomalies (not shown) also show an equatorially trapped anomaly, of opposite sign to the SLP anomaly, that propagates eastward over the Pacific. Figure 9 shows a vertical cross-section of geopotential height anomalies along the equator on Day −4. Over the Pacific, the vertical structure is one of opposite sign between the upper and lower troposphere, with a phase reversal near the 400-mb level, consistent with the propagating deep convective mode of Neelin and Yu (1994). There is also a further reversal at the tropopause with anomalies of opposite sign in the lower stratosphere. Phase lines over the western Pacific (150°E) are approximately horizontal indicating no vertical propagation. Over the eastern Pacific and at the longitude of the Andes (80°W), there is an eastward phase tilt with height, indicating upward group velocity (Andrews *et al.* 1987). It appears that the Kelvin wave propagates horizontally along the equator over the Pacific until the wavefront reaches the Andes, where it is partitioned into vertically, meridionally and eastward-propagating parts.

The mass circulation of the "positive" Kelvin wave propagating across the Pacific will have a downwelling wavefront, with descent throughout the troposphere (Heckley and Gill 1984). When the wavefront reaches the Andes it appears to suppress convection there, as indicated by the positive equatorial OLR anomaly from Day −4 to Day 0 at 80°W (Fig. 8). There also appears to be an interaction between the Kelvin wave structure and convection over the Pacific ITCZ with enhanced convection coincident with the negative SLP anomaly and anomalous low-level easterlies from Day −8 to Day 0. This is discussed in the next section.

7. Interaction Between Circulation and Convection

Emanuel (1987) proposed a model of the MJO using the Quasi-Equilibrium theory of convection, where convection acts to rapidly redistribute changes to the boundary-layer moist entropy throughout the troposphere, rather than acting as an externalised heat source *per se* (Emanuel *et al.* 1994). An eastward-propagating equatorial Kelvin wave will have associated surface easterly wind anomalies and positive mid-tropospheric temperature anomalies to the east of its ascent region, and surface westerly anomalies and negative mid-tropospheric temperature anomalies to the west. The enhanced convection in the ascent region reduces the effective static stability felt by the Kelvin wave and slows its speed down from that of the dry Kelvin wave. If a finite time-lag is introduced between the ascent and the convection, then the convective heating will be biased towards the region of negative mid-tropospheric temperature anomaly to the west of the ascent region, and the mode will be damped (Emanuel 1993).

However, if the basic state is one of mean surface easterlies, then the total surface wind speed, and hence the surface latent heat flux and the boundary-layer moist entropy, will increase to the east of the ascent region, and decrease to the west. Convection will then rapidly adjust the temperature of the free troposphere, and the positive (negative) mid-tropospheric temperature anomalies to the east (west) of the ascent region will be amplified and the mode will grow. The effect of this air-sea interaction or Wind Induced Surface Heat Exchange (WISHE) can be greater than the damping due to the time-lag between ascent and convection, and the overall mode can grow. A similar model was also proposed by Neelin *et al.* (1987).

Figure 10 shows the mean zonal wind at 850 mb from the perpetual March integration (surface winds were not available). The tropical central and eastern Pacific are

indeed a region of low-level easterlies, but there is a substantial region of low-level westerly flow over the Indian Ocean and western Pacific. Hence WISHE may be relevant for the growth and eastward propagation of the convective anomalies over the central and eastern Pacific, but not over the western Pacific (Wang 1988).

Figure 11 shows regressed fields of surface latent heat flux anomalies for two selected days in the simulated MJO cycle. Comparison with the OLR anomalies in Fig. 6 and 850-mb streamfunction anomalies in Fig. 7 indicates the role of the surface latent heat flux in the simulated MJO. On Day -12 there is a large region of enhanced convection over the tropical Indian Ocean, mainly south of the equator. This is accompanied by an 850-mb cyclonic anomaly, which can be interpreted as an equatorial Rossby wave associated with the enhanced convection. The 850-mb cyclonic anomaly has anomalous westerlies on its equatorward side (from the equator to 10°S) and anomalous easterlies on its poleward side (from 20°S-30°S). Comparison with Fig. 10 shows that this anomalous flow is of the same sign as the mean 850-mb flow, hence the total low-level flow will be enhanced over this whole region. Therefore, there is a positive anomaly of surface latent heat flux on Day -12 over the Southern Hemisphere tropical Indian Ocean (Fig. 11a), and the positive convective anomaly over the Indian Ocean is reinforced. This self-consistent cycle of convection and its associated anomalous low-level flow, which, together with the mean low-level flow, acts to enhance the surface latent heat flux and sustain the convection, may help to explain the persistence of this convective anomaly, from Day -15 to Day -4. As the mean near-equatorial flow is near zero over the Indian Ocean, under WISHE the convective anomaly would not move either eastward or westward and, indeed, it does grow and decay in situ.

Further to the east, near 150°E in the western Pacific, there is a region of strong mean low-level westerlies on the equator (Fig. 10). On Day -12 there are anomalous low-level equatorial easterlies over this region (Fig. 7), possibly a Kelvin wave associated with the enhanced convection over the Indian Ocean. These anomalous easterlies will reduce the total wind speed and hence the surface latent heat flux (Fig. 11a) and help to account for the region of reduced convection over the western Pacific, i.e., the other half of the convective dipole.

By Day -4, the "positive" Kelvin wave has propagated rapidly along the equator from the western Pacific (Fig. 8) and there are strong anomalous low-level easterlies over the whole of the tropical Pacific (Fig. 7). These reinforce the mean low-level easterlies over the central and eastern Pacific and lead to the strongly enhanced surface latent heat flux there (Fig. 11b). This, in turn, is likely to account for the enhanced convection along the Pacific ITCZ on Day -4 (Fig. 8). In the latter half of the life-cycle, a "negative" dry Kelvin wave propagates rapidly across the Pacific. The anomalous surface westerlies associated with this Kelvin wave then decrease the total surface wind speed and hence the total surface latent heat flux over the Pacific (not shown), leading to reduced convection in the ITCZ region.

8. Slow Equatorial Kelvin Wave Structures

As noted above, the dry Kelvin wave propagates eastward over the Pacific at a speed of around 55 m s^{-1}, much faster than the 15 m s^{-1} average speed of the MJO "mode". It is of interest to ask whether Kelvin wave dynamics can account for this slower eastward propagation of the MJO mode. A practical diagnostic to isolate a Kelvin wave signal is to split the divergence into its two components, $\partial u/\partial x$ and $\partial v/\partial y$. As an idealised Kelvin wave has zero meridional wind perturbation, then if the simulated MJO has a large Kelvin wave component, the divergence field associated with the MJO may be

expected to be comprised mainly of a $\partial u/\partial x$ contribution, with only a small amplitude $\partial v/\partial y$ contribution.

The development of the divergent wind field anomalies in the equatorial band (10°N-10°S) through a life-cycle of the simulated MJO is shown in the time-longitude diagrams of Fig. 12. The zonal wavenumber one signal in 200-mb velocity potential is clearly shown in Fig. 12a. The wave propagates eastward around the equator in 30 days, amplifying as it passes over the convectively active regions of the western Indian Ocean, the western Pacific, and South America.

The equatorial 200-mb divergence anomaly is shown in Fig. 12b. As velocity potential is the inverse Laplacian of divergence, the velocity potential field is a measure of the planetary-scale divergence field, with a sign reversal. Hence, to aid comparison between the two fields, negative 200-mb velocity potential anomalies are shaded in Fig. 12a, and positive 200-mb divergence anomalies are shaded in Fig. 12b. The equatorial 200-mb divergence structure shows the same basic zonal wavenumber one eastward-propagating wave as the velocity potential structure, but with more small-scale structure.

To emphasise the larger scales, Fig. 12c also shows the equatorial 200-mb divergence anomaly, but only retaining zonal wavenumbers 0 to 3. The relationship between the equatorial velocity potential in Fig. 12a and the equatorial divergence in Fig. 12b can be seen more clearly if it is interpreted via this "intermediate" smoothed equatorial divergence field in Fig. 12c. Figures. 12d and 12e show the two components of the 200-mb divergence anomaly, $\partial u/\partial x$ and $\partial v/\partial y$ respectively. Only zonal wavenumbers 0 to 3 have been retained. The two components have similar amplitude, hence the equatorial MJO structure is certainly not a pure Kelvin wave. However, the zonal wavenumber one eastward-propagating wave is clearly present in the $\partial u/\partial x$ structure, but $\partial v/\partial y$ has no easily discernible propagating features. Hence the eastward-propagating zonal wavenumber one divergence wave is comprised mainly of the $\partial u/\partial x$, rather than the $\partial v/\partial y$ component, in favour of an underlying Kelvin wave mechanism for the simulated MJO.

A similar analysis of the divergence field at 850 mb now follows. Fig. 12f shows the 850-mb equatorial velocity potential anomaly, with positive values shaded. It closely resembles the 200-mb equatorial velocity potential anomaly, but with reversed sign and smaller amplitude (the contour interval in Fig. 12f is half that in Fig. 12a). Unlike at 200 mb, the divergence anomaly at 850 mb (Figs. 12g,h) does not show an obvious eastward-propagating wave.

However, when the 850-mb divergence is split into its $\partial u/\partial x$ and $\partial v/\partial y$ components (Figs. 12i and 12j, respectively), a weak eastward-propagating signal emerges in both fields. The eastward-propagating signal in the $\partial u/\partial x$ anomaly is in phase with the 850-mb velocity potential anomaly (Fig. 12f) and is probably related to the Kelvin wave. However, the eastward-propagating signal in the 850-mb $\partial v/\partial y$ anomaly is approximately out of phase with that of the 850-mb $\partial u/\partial x$ anomaly and this partial cancellation masks any eastward-propagating signal in the total 850-mb divergence anomaly (Figs. 12g,h). A comparison of Fig. 7 and Figs. 12e,j shows that the 200-mb and 850-mb $\partial v/\partial y$ anomalies are consistent with equatorial Rossby wave structures over the Eastern Hemisphere.

The arrival and stalling of the dry Kelvin wavefront at the Andes can clearly be seen in the negative 200-mb divergence anomalies at 80°W from around Day -8 to Day $+8$ (Fig. 12b) These are associated with the reduced convection (negative OLR anomalies) over the region in Fig. 8. Examination of the $\partial u/\partial x$ and $\partial v/\partial y$ anomalies (with all zonal wavenumbers included, not shown) reveals that this is composed mainly of a negative $\partial u/\partial x$ component (probably due to the equatorial Kelvin wave). However, this negative 200-mb divergence anomaly also has a negative $\partial v/\partial y$ component. This may arise from

a poleward-propagating Kelvin wave trapped against the Andes.

9. Discussion

The UKMO Unified Model (UM) has been integrated for 1800 days with perpetual March boundary conditions. A coherent MJO was found in the integration and its structure analysed. The simulated MJO was found to have a zonal wavenumber one structure in 200-mb velocity potential that propagated eastward around the equator at an average speed of 15 m s^{-1}, taking approximately 30 days to complete a circuit. An EOF analysis of 200-mb velocity potential was used as the basis for a regression analysis to determine the structure of the simulated MJO in other variables. In the tropics, the vertical structure was baroclinic, with velocity potential anomalies of very similar horizontal structure but of opposite sign in the upper and lower troposphere. Regions of large-scale upper-tropospheric divergence and lower-tropospheric convergence, with inferred mid-tropospheric ascent, were associated with positive convective anomalies. Rather than propagating eastward, the convective anomalies tended to grow and decay *in situ*. New anomalies developed to the east of the old ones, with the result that a large-scale envelope of convection moved eastward.

The divergence and convective signals were accompanied by a coherent signal in the rotational wind field. A predominantly zonal wavenumber two tropical streamfunction signal also moved eastward. A pair of 200-mb anticyclonic anomalies lay either side of the equator alongside, or to the west of, the positive convective anomalies. To the east, a cyclonic anomaly lay either side of the equator. In the extratropics, a wavetrain arced over the North Pacific and North America.

At 850 mb, the wind anomalies were of opposite sign in the tropics, such that 200-mb equatorial easterly (westerly) anomalies were found above 850-mb equatorial westerly (easterly) anomalies. In the extratropics, the streamfunction anomalies had a more equivalent barotropic structure, such that the wavetrain over the North Pacific and North America had the same sign anomalies throughout the troposphere.

Overall, the simulated MJO, as described above, is very similar to the observed MJO, and is consistent with the convectively active Rossby-Kelvin wave paradigm over the Eastern Hemisphere. However, there are also differences. Primarily, the simulated convection over the warm pool region was much weaker than in observations, both in the mean and the MJO. This may be due to the diurnal cycle in SST and the implied warmer skin temperatures in light wind conditions, as would occur over the warm pool (Webster *et al.* 1996). This diurnal cycle was not represented in the UM. Also, the characteristics of convection over the Indian Ocean differed between the model and observations. The fluctuations in convection occured on the edge of the area of mean convection in the UM, but near the centre of the area of mean convection in observations.

In common with nearly all other simulations of the MJO, the phase speed was too fast. In this particular integration, this could be due to the lack of convection over the warm pool and lack of anomalous convection near the equator over the Indian Ocean. Within the context of the coupled moist Rossby-Kelvin mode paradigm, the mode propagates more slowly over the convective regions of the Indian Ocean and the western Pacific, and faster over the drier regions of the eastern Pacific and the Atlantic. If a convective region is absent or weakened, as in the case of the warm pool, then the average eastward speed of the MJO will be faster, and the period will be decreased.

Therefore, it may be necessary to obtain the correct convective characteristics over the warm pool region, to make the simulated MJO more realistic in terms of its structure over this region, and in its overall period. More realistic convection over the warm pool

may also give a more realistic simulation of the position of the East Asian jet, which is situated slightly northeast of the observed jet. Such a change in the basic state is likely to affect the exact position and strength of the North Pacific wavetrain that accounts for much of the extratropical part of the MJO.

Another possibility for the difference between the observed and modeled phase speeds could be feedback with the ocean. A study of the NCEP/NCAR reanalysis dataset showed negative SST anomalies to the west of the MJO convection and positive SST anomalies to the east (Sperber *et al.* 1997). The negative SST anomalies were attributed to the strong surface westerlies and associated increased evaporation and vertical mixing, together with a reduction in surface solar fluxes due to the increased cloudiness west of and coincident with the MJO convection (Flatau *et al.* 1996). To the east of the MJO convection, the SST increased in the region of weaker surface (easterly) winds and clear skies. When this atmosphere-ocean feedback effect was incorporated into a GCM, the period of the simulated MJO increased from around 30 days to near 60 days, in agreement with observations.

The spectral characteristics of the MJO in the perpetual March UM integrations were compared with those from an AMIP integration of the UM. The perpetual March integration showed a distinct peak in the equatorial zonal wavenumber one velocity potential field, with a period near 30 days. The AMIP integration also had this peak, but had additional power at lower intraseasonal frequencies, near the observed peak of 40–60 days. Therefore, it is possible that the annual cycle and/or interannual forcing may be a factor in simulating the correct period of the MJO. Analysis of the MJO in an integration of the UM with a fixed annual cycle, but no interannually varying boundary conditions, could help to answer this question.

The appearance of the MJO in the 1800-day perpetual March integration was rather sporadic, with long periods of very little intraseasonal activity. This sporadic behaviour, or low-frequency modulation, of the MJO must be internally generated, as the boundary conditions are constant, and deserves further investigation. A study of the interannual variability of the MJO in an ensemble of extended integrations of the UM, using observed SSTs to force the model, found only a weak relationship with SST (Slingo *el al* 1998), consistent with the conclusion from the perpetual March integration that the low-frequency variability of the MJO is internally generated.

Equatorial Kelvin waves appear to play an important role in the dynamics of the simulated MJO. Fast equatorial Kelvin waves over the Pacific, with phase speeds near 40 m s^{-1} and first-internal mode vertical structures in the troposphere, have been observed in the real atmosphere. These fast Kelvin waves have the same phase relation to the observed MJO as they do in the simulated MJO described in this paper, with a pulse of negative SLP anomalies propagating eastward across the equatorial Pacific as the intraseasonal convective anomalies change sign in the western Pacific (Millif and Madden 1996). The observed equatorial SLP pulse was also stopped by the Andes, and then propagated polewards into both hemispheres trapped against the west coast of the Americas (Weickmann *et al.* 1997).

The Andes and the mountains of Central America act as a rather efficient barrier to the observed SLP anomaly, the only evidence of any through-flow is near Panama (Weickmann *et al.* 1997). This is in contrast to the behaviour in the UM, where a significant SLP anomaly crosses the mountains and propagates eastward along the equator from the Andes. The cause of this discrepancy between the observed and modeled behaviour of the SLP anomaly may be due to the resolution of the topography in the UM, which will act as a rather "leaky" barrier and will underestimate the torque applied to the model atmosphere. This mountain torque, arising from the pressure gradient exerted by

the mass field of the equatorial Kelvin wave as it is blocked by the Andes, is a major component of the AAM budget of the observed MJO (Weickmann *et al.* 1997). For this AAM cycle to be accurately simulated, higher resolution, or envelope, orography may be needed.

Regression maps of surface latent heat flux and convection over the Pacific indicated that WISHE could be instrumental in the shift of the simulated MJO convective anomalies into the eastern Pacific. The surface easterly anomalies on the equator, associated with the "positive" Kelvin wave associated with anomalous heating over the Indian Ocean, act to increase the mean surface easterlies over the equatorial eastern Pacific. This increases the surface latent heat flux, especially over the warm SSTs of the ITCZ, and hence positive convective anomalies arise along the central and eastern Pacific ITCZ. Although the WISHE mechanism appears to be important over the eastern Pacific in the GCM, its role in the real atmosphere is still unclear and deserves further study.

WISHE does not appear to account for the eastward development of convection from the Indian Ocean to the western Pacific in the model. The mean surface winds are near zero or westerly in this region and enhanced surface heat flux is coincident with the anomalous convection, which grows and decays *in situ*. Indeed, latent heat flux anomalies to the east of the enhanced convection in the Indian Ocean are negative (Fig. 11a), indicating that WISHE is not the dominant mechanism of eastward propagation in this region. This is in agreement with the observational and GCM results of Sperber *et al.* (1997).

An apparent disagreement between the fast Kelvin wave propagation over the Pacific at a phase speed consistent with a dry static stability and the existence of moist convective anomalies over the region may be explained by a lag between the Kelvin wave and the convection. When the Kelvin wave propagates across the Pacific between Day -10 and Day -6 (Fig. 8) there is little deep convection near the wavefront, so the Kelvin wave propagates at approximately the dry phase speed of 55 m s^{-1}. The convective anomalies over the Pacific peak several days later at Day 0, presumably as a WISHE response to the enhanced surface easterlies associated with the Kelvin wave.

The planetary wavenumber scale selection of the simulated MJO is also consistent with WISHE. Although there are no explicit assumptions of quasi-equilibrium in the convective scheme of the UM, a quasi-equilibrium structure between convection and large-scale forcing is established (Gregory and Rowntree 1990). Quasi-equilibrium theory predicts that all moist convective modes will be damped, though low wavenumber modes will only be weakly damped. If the effects of WISHE are included, these low wavenumber modes can be destabilised (Neelin and Yu 1994). Alternatively, Salby and Garcia (1987) showed that an initial Kelvin wave packet associated with tropical convection would disperse vertically, such that the high wavenumber components will propagate preferentially into the stratosphere leaving the low wavenumber components in the troposphere.

To isolate the existence of an equatorial Kelvin wave structure over the whole MJO life-cycle, the equatorial divergence anomaly was decomposed into its $\partial u/\partial x$ and $\partial v/\partial y$ components. As a Kelvin wave has zero meridional wind anomaly, the $\partial u/\partial x$ term would be expected to be larger than the $\partial v/\partial y$ term if a Kelvin wave structure was dominant. Results showed that the $\partial u/\partial x$ and $\partial v/\partial y$ terms had approximately equal magnitudes. However, the eastward-propagating part of the divergence anomalies tended to be composed mainly of the $\partial u/\partial x$ component, both in the upper and lower troposphere. The $\partial v/\partial y$ component tended to disrupt this eastward propagation. The behaviour of the $\partial u/\partial x$ anomalies supports the paradigm of an underlying Kelvin wave mechanism for the eastward propagation of the MJO, but it is clear from the equally important $\partial v/\partial y$ anomalies that other factors such as an equatorial Rossby wave component are involved.

A similar analysis of the divergence components in the observed MJO would help to resolve this question.

Acknowledgement

The authors would like to thank George Kiladis and two anonymous referees for useful comments that improved the original manuscript. NCEP/NCAR reanalysis data was provided through the NOAA Climate Diagnostics Centre (http://www.cdc.noaa.gov). The NCEP/NCAR potential vorticity data was calculated by George Kiladis. The UM integration was performed on computers at the Hadley Centre under the auspices of the European Climate Computer Network. This research was supported by the Natural Environment Research Council under Grant GST/02/805.

References

Andrews, D. G., Holton, J. R. and Leovy, C. B 1987 *Middle Atmosphere Dynamics*, Academic Press, Orlando

Barnston, A. G. and Livezey, R. E. 1987 Classification, seasonality and persistence of low frequency atmospheric circulation patterns. *Mon. Weather Rev.*, **115,** 1083–1126

Cullen, M. J. P. 1993 The unified forecast/climate model. *Meteorol. Mag.*, **122,** 91–94

Duchon, C. E. 1979 Lanczos filtering in one and two dimensions. *J. Appl. Meteorol.*, **18,** 1016–1022

Emanuel, K. A. 1987 An air-sea interaction model of intraseasonal oscillations in the tropics. *J. Atmos. Sci.*, **44,** 2324–2340

Emanuel, K. A. 1993 The effect of convective response time on WISHE modes. *J. Atmos. Sci.*, **50,** 1763–1775

Emanuel, K. A., Neelin, J. D. and Bretherton, C. S. 1994 On large-scale circulations in convecting atmospheres. *Q.J.R. Meteorol. Soc.*, **120,** 1111–1143

Ferranti, L., Palmer, T. N., Molteni, F. and Klinker, E. 1990 Tropical-extratropical interaction associated with the 30-60 day oscillation and its impact on medium and extended range prediction. *J. Atmos. Sci.*, **47,** 2177–2199

Flatau, M., Flatau, P. J., Phoebus, P. and Niiler, P. P. 1997 The feedback between equatorial convection and local radiative and evaporative processes: The implications for intraseasonal oscillations. *J. Atmos. Sci.*, **54,** 2373–2386

Gregory, D. and Rowntree, P. R. 1990 A mass flux convection scheme with representation of cloud ensemble characteristics and stability dependent closure. *Mon. Weather Rev.*, **118,** 1483–1506

Heckley, W. A. and Gill, A. E. 1984 Some simple analytical solutions to the problem of the forced equatorial long waves. *Q.J.R. Meteorol. Soc.*, **110,** 203–217

Hendon, H. H. and Salby, M. L. 1994 The life cycle of the Madden-Julian oscillation. *J. Atmos. Sci.*, **51,** 2225–2237

Hsu, H. -H., Hoskins, B. J. and Jin F. -F. 1990 The 1985/86 intraseasonal oscillation and the role of the extratropics. *J. Atmos. Sci.*, **47,** 823–839

Inness, P. M. and Gregory, D. 1997 Aspects of the intraseasonal oscillation simulated by the Hadley Centre atmospheric model. *Climate Dynamics*, **13,** 441–458

Kalnay, E., Kanamitsu, M., Kistler, R., Collins, W., Deaven, D., Gandin, L., Iredell, M., Saha, S., White, G., Woollen, J., Zhu, Y., Chelliah, M., Ebisuzaki, W., Higgins, W., Janowiak, J., Mo, K. C., Ropelewski, C., Wang, J., Leetma, A., Reynolds, R., Jenne, R. and Joseph, D. 1996 The NCEP/NCAR 40-year reanalysis project. *Bull. Am. Meteorol. Soc.*, **77,** 437–471

Kiladis, G. N. and Weickmann, K. M.	1992	Circulation anomalies associated with tropical convection during northern winter. *Mon. Weather Rev.*, **120,** 1900–1923
Knutson, T. R. and Weickmann, K. M.	1987	30-60 day atmospheric oscillations: composite life cycles of convection and circulation anomalies. *Mon. Weather Rev.*, **115,** 1407–1436
Lau, K. -M. and Chan, P. H.	1983	Short term climate variability and atmospheric teleconnections from satellite observed outgoing longwave radiation. Part I: Simultaneous relationships. *J. Atmos. Sci.*, **40,** 2735–2750
Lau, K. -M. and Phillips, T. J.	1986	Coherent fluctuations of extratropical geopotential height and tropical convection in intraseasonal time scales. *J. Atmos. Sci.*, **43,** 1164–1181
Liebmann, B. and Smith, C. A.	1996	Description of a complete (interpolated) OLR dataset. *Bu. Amer. Meteorol. Soc.*, **77,** 1275–1277
Livezey, R. E., and Chen, W. Y.	1983	Statistical field significance and its determination by Monte Carlo techniques. *Mon. Weather Rev.*, **111,** 46–59
Lorenc, A. C.	1984	The evolution of planetary scale 200 mb divergent flow during the FGGE year. *Q.J.R. Meteorol. Soc.*, **110,** 427–441
Madden, R. A. and Julian, P. R.	1971	Detection of a 40-50 day oscillation in the zonal wind in the tropical Pacific. *J. Atmos. Sci.*, **28,** 702–708
Madden, R. A. and Julian, P. R.	1972	Description of global scale circulation cells in the tropics with a 40-50 day period. *J. Atmos. Sci.*, **29,** 1109–1123
Matthews, A. J.	1993	*The intraseasonal oscillation.* Ph.D. thesis. University of Reading
Milliff, R. F. and Madden, R. A.	1996	The existence and vertical structure of fast, eastward-moving disturbances in the equatorial troposphere. *J. Atmos. Sci.*, **53,** 586–597
Neelin, J. D., Held, I. M. and Cook, K. H.	1987	Evaporation-wind feedback and low frequency variability in the tropical atmosphere. *J. Atmos. Sci.*, **44,** 2341–2348
Neelin, J. D. and Yu, J.	1994	Modes of tropical variability under convective adjustment and the Madden-Julian oscillation. Part I: Analytical results. *J. Atmos. Sci.*, **51,** 1876–1894
Rui, H. and Wang, B.	1990	Development characteristics and dynamic structure of tropical intraseasonal convective anomalies. *J. Atmos. Sci.*, **47,** 357–379
Salby, M. L. and Garcia, R. R	1987	Transient response to localized episodic heating in the tropics. Part I: Excitation and short-time near field behaviour. *J. Atmos. Sci.*, **44,** 458–498
Salby, M. L. and Hendon, H. H.	1994	Intraseasonal behaviour of clouds, temperature, and motion in the tropics. *J. Atmos. Sci.*, **51,** 2207–2224
Slingo, J. M. and Madden, R. A.	1991	Characteristics of the tropical intraseasonal oscillation in the NCAR community climate model. *Q.J.R. Meteorol. Soc.*, **117,** 1129–1169
Slingo, J. M., Rowell, D. P., Sperber, K. R. and Nortley, F.	1998	On the predictability of the interannual behaviour of the Madden-Julian oscillation and its relationship to El Niño. To appear in *Q.J.R. Meteorol. Soc.*
Slingo, J. M., Sperber, K. R., Boyle, J. S., Ceron, J. -P., Dix, M., Dugas, B., Ebisuzaki, W., Fyfe, J., Gregory, D., Gueremy, J.- F., Hack, J., Harzallah, A., Inness, P., Kitoh, A., Lau, W. K. -M., McAvaney, B., Madden, R., Matthews, A., Palmer, T. N., Park, C. -K., Randall, D. and Renno, N.	1996	Intraseasonal oscillations in 15 atmospheric general circulation models: results from an AMIP diagnostic subproject. *Climate Dynamics*, **12,** 325–358
Sperber, K. R., Slingo, J. M., Inness, P. M. and Lau, W. K. -M.	1997	On the maintenance and initiation of the intraseasonal oscillation in the NCEP/NCAR reanalysis and the GLA and UKMO AMIP simulations. *Climate Dynamics*, **13,** 769–795

Wang, B.	1988	Comments on "An air-sea interaction model of the intraseasonal oscillation in the tropics". *J. Atmos. Sci.*, **45,** 3521–3525
Webster, P. J., Clayson, C. A. and Curry, J. A.	1996	Clouds, radiation, and the diurnal cycle of sea surface temperature in the tropical western Pacific. *J. Climate*, **9,** 1712–1730
Weickmann, K. M., Kiladis, G. N. and Sardeshmukh, P. D.	1997	The dynamics of intraseasonal atmospheric angular momentum oscillations. *J. Atmos. Sci.*, **54,** 1445–1461
Zhang, C. D. and Hendon, H. H.	1997	Propagating and standing components of the intraseasonal oscillation in tropical convection. *J. Atmos. Sci.*, **54,** 741–752

Figure 1. Mean OLR: (a) simulated, (b) observed February-March 1979-95; contour interval is 20 W m^{-2} and values below 260, 240, 220 and 200 W m^{-2} are shaded with increasing darkness. Mean 200-mb zonal wind: (c) simulated, (d) observed February-March 1979-95; contour interval is 10 m s^{-1}; easterlies are shaded lightly, and westerlies above 30 and 50 m s^{-1} are shaded darkly. Mean 350K potential vorticity: (e) simulated, (f) observed February-March 1979-95; contour interval is 1x10^{-6} $m^2 kg^{-1} s^{-1} K^{-1}$ or 1 PVU; the zero contour is thickened; values above 3 and 7 PVU are shaded lightly and values below -3 and -7 PVU are shaded darkly.

Figure 2. Power spectra of zonal wavenumber one 200-mb equatorial velocity potential: (a) NCEP/NCAR reanalyses (solid line), (b) AMIP simulation (dotted line), (c) perpetual March simulation (dashed line). Positive (negative) frequency indicates eastward- (westward-) propagating waves.

Figure 3. Time-longitude diagram of 20-100 day filtered 200-mb equatorial (10°N–10°S) velocity potential from days 100 to 1700 of the perpetual March simulation. Contour interval is 2×10^6 m^2 s^{-1}; the zero contour is omitted; values below -2×10^6 m^2 s^{-1} are shaded darkly, and values above $+2 \times 10^6$ m^2 s^{-1} are shaded lightly.

Figure 4. (a) EOF1 and (b) EOF2 of 20-100 day bandpass filtered 200-mb velocity potential. Contour interval is 4×10^5 m^2 s^{-1}, and negative values are shaded.

Figure 5. Principal component time series of EOF1 (solid line) and EOF2 (dashed line).

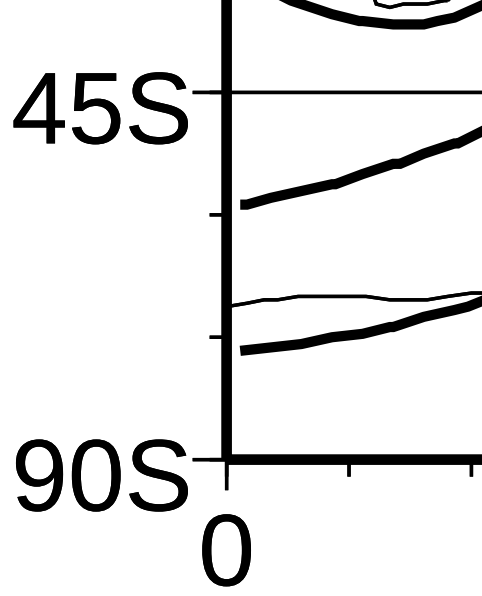

Figure 6. Lagged regression maps of OLR and 200-mb velocity potential anomalies, corresponding to a value of 2.0 of the reference time series PC1. All fields have been passed through a 20-100 day filter. OLR is shaded darkly below -8 W m^{-2}, and lightly above +8 W m^{-2}. Contour interval for 200-mb velocity potential is 1x10^6 m^2 s^{-1}; positive (negative) contours are solid (dashed).

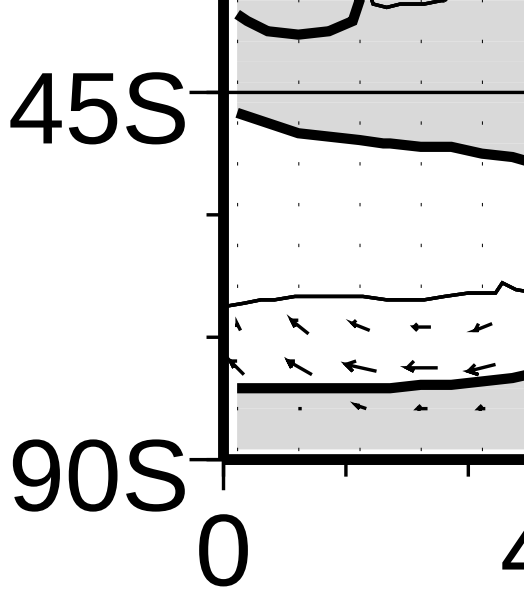

Figure 7. As in Fig. 6, but for 200-mb and 850-mb streamfunction and wind vector anomalies. Contour interval is 2×10^6 m^2 s^{-1} (1×10^6 m^2 s^{-1}) for 200-mb (850-mb) streamfunction, and negative values are shaded. Wind vectors are plotted where either the u or v component of the wind is locally significant at the 95% level; peak vectors of the 200-mb (850-mb) wind are approximately 10 m s^{-1} (5 m s^{-1}).

Figure 8. As in Fig. 6, but for OLR and SLP anomalies. OLR is contoured heavily; contour interval is 8 W m^{-2}; positive (negative) contours are solid (dashed), and the zero contour is suppressed. SLP is contoured lightly; contour interval is 40 Pa, and negative values are shaded.

Figure 9. As in Fig. 6, but for longitude-pressure cross-section of geopotential height anomalies at the equator on Day −4. Contour interval is 2 m and negative values are shaded.

Figure 10. Mean zonal wind at 850 mb. Contour interval is 5 m s^{-1}, and easterlies are shaded.

Figure 11. As in Fig. 6, but for surface latent heat flux anomalies on (a) Day −12 and (b) Day −4. Contour interval is 10 W m^{-2}; positive (negative) contours are solid (dashed), and the zero contour is suppressed. Shading indicates local significance at the 95% level.

Figure 12. As in Fig. 6, but for time-longitude diagrams of: (a) 200-mb velocity potential anomalies; contour interval is 2x10^6 m^2 s^{-1} and negative values are shaded, (b) 200-mb divergence anomalies; contour interval is 4x10^{-7} s^{-1} and positive values are shaded. 200-mb (c) divergence, (d) ∂u/∂x and (e) ∂v/∂yanomalies; only zonal wavenumbers 0-3 are retained; contour interval is 2x10^{-7} s^{-1} and positive values are shaded. (f) 850-mb velocity potential anomalies; contour interval is 1x10^6 m^2 s^{-1} and positive values are shaded, (g) 850-mb divergence anomalies; contour interval is 2x10^{-7} s^{-1} and negative values are shaded. 850-mb (h) divergence, (i) ∂u/∂x and (j) ∂v/∂yanomalies; only zonal wavenumbers 0-3 are retained; contour interval is 1x10^{-7} s^{-1} and negative values are shaded.